Electronic Supplementary Information

Rutile-Type Metal Dioxide (110) Surfaces for the Cyclic Oxidation of Methane to Methanol

Farrel Dzaudan Naufal,[a] Hasna Afifah,[b] Marleni Wirmas,[b] Mohammad Kemal Agusta,[a,c] Adhitya Gandaryus Saputro,[a,c] Hadi Teguh Yudistira,[d] Aleksandar Staykov,[e] Kazunari Yoshizawa,[f] and Muhammad Haris Mahyuddin,*[,a,c]

[a] Quantum and Nano Technology Research Group, Faculty of Industrial Technology, Institut Teknologi Bandung, Jl. Ganesha 10 Bandung 40132, Indonesia

[b] Doctoral Program of Engineering Physics, Faculty of Industrial Technology, Institut Teknologi Bandung, Jl. Ganesha 10 Bandung 40132, Indonesia

[c] Research Center for Nanoscience and Nanotechnology, Institut Teknologi Bandung, Jl. Ganesha 10 Bandung 40132, Indonesia

[d] Mechanical Engineering Study Program, Institut Teknologi Sumatera, Way Hui, South Lampung 35365, Indonesia

[e] International Institute for Carbon-Neutral Energy Research, Kyushu University, Fukuoka 819-0395, Japan

[f] Fukui Institute for Fundamental Chemistry, Kyoto University, Sakyo-ku, Kyoto 606-8103, Japan

* To whom all correspondences should be addressed

(e-mail: mahyuddin133[at]itb.ac.id).

Table of Contents:

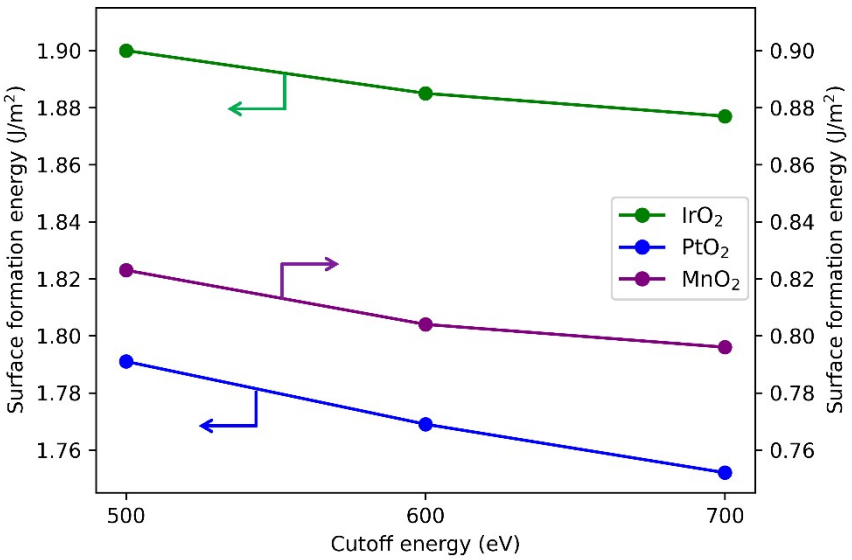

Figure S1. Surface formation energy of clean IrO_2(110), β-PtO_2(110), and β-MnO_2(110) surfaces calculated using different cut-off energy values.

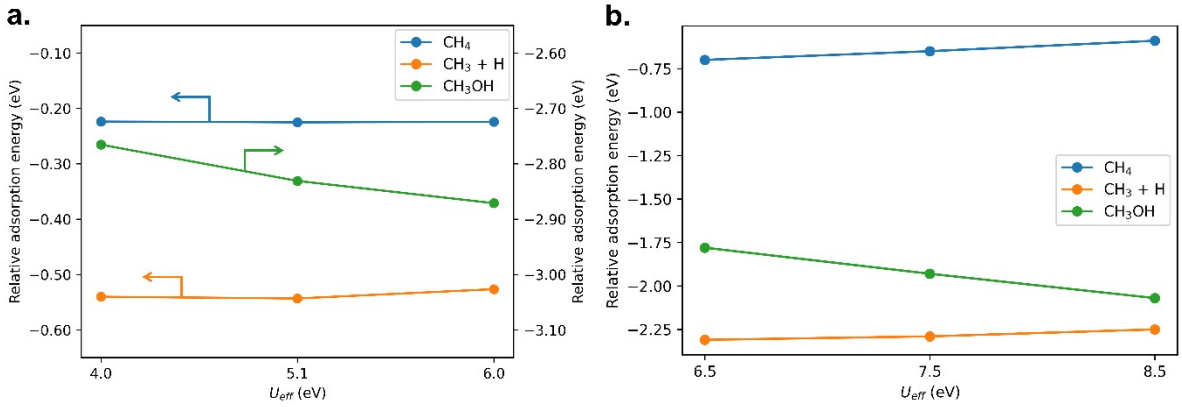

Figure S2. Relative energies of the CH_4, Mn⋯•CH_3+H or Pt–CH_3+H, and CH_3OH adsorption on the (a) β-MnO_2(110) and (b) β-PtO_2(110) surfaces calculated using different U_{eff} values.

The use of U_{eff} = 5.1 and 7,5 eV for Mn 3d and Pt 5d orbitals, respectively, is chosen according to two thorough investigations reported by Tompsett et al. (*J. Am. Chem. Soc.* 2014, 136, 4, 1418–1426) and Tsuji et al. (*ACS Omega* 2021, 6, 21, 13858–13869). In these reports, the authors carefully tested various U_{eff} values and found optimized values that can correctly treat the strong correlation effects of Mn^{4+}, Mn^{3+}, Pt^{4+}, and Pt^{3+} involved in the present study. Figures above also show that the use of different U values insignificantly alters the relative adsorption energies.

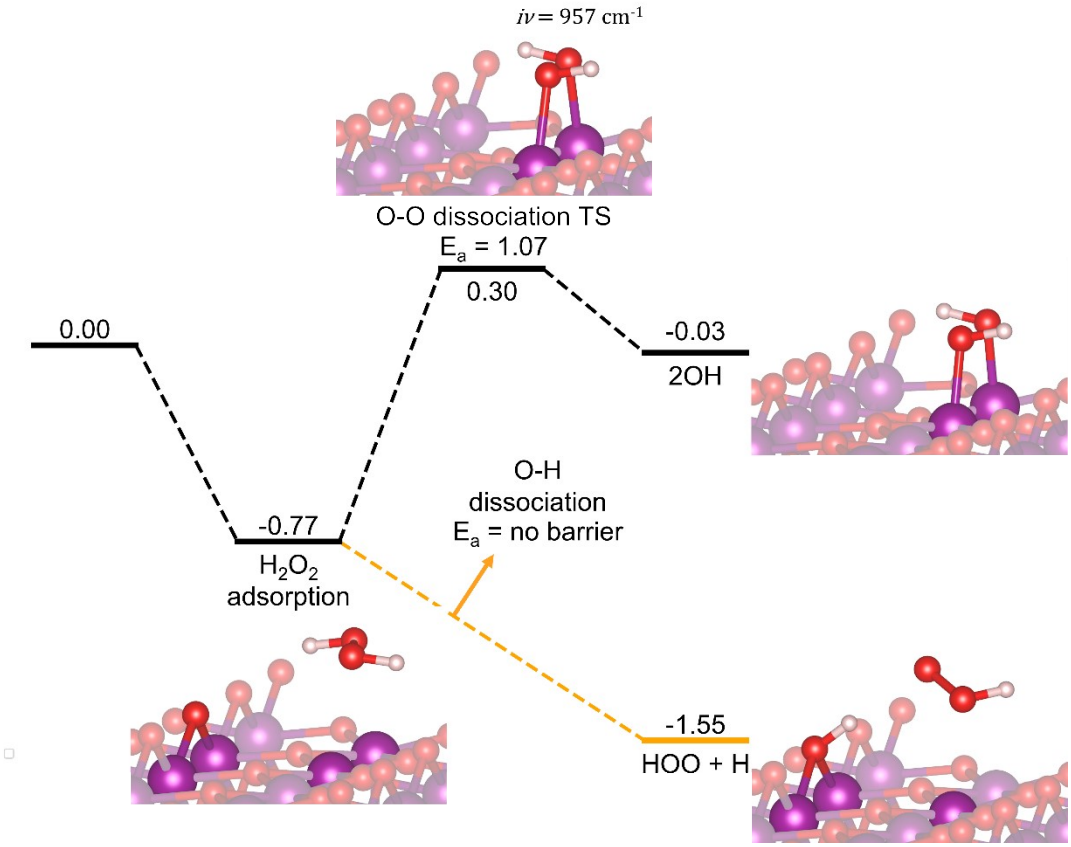

Figure S3. Energy diagrams (in eV) of H_2O_2 decomposition on the stoichiometric β-MnO_2(110) surface via the O–O and O–H bond scission pathways.

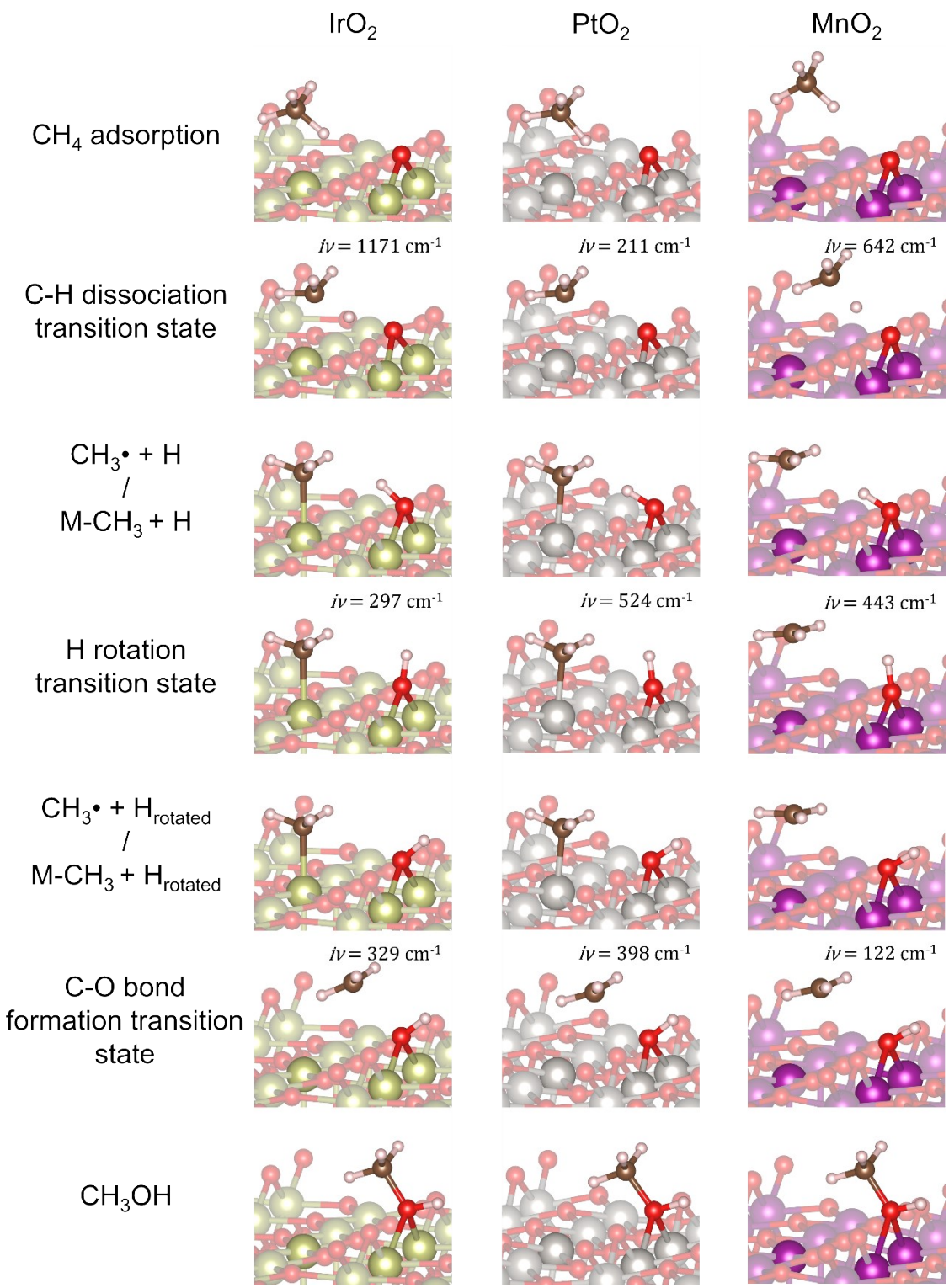

Figure S4. Geometrical structures of each reaction step of the methane to methanol conversion on the stoichiometric $IrO_2(110)$, β-$PtO_2(110)$, and β-$MnO_2(110)$ surfaces.

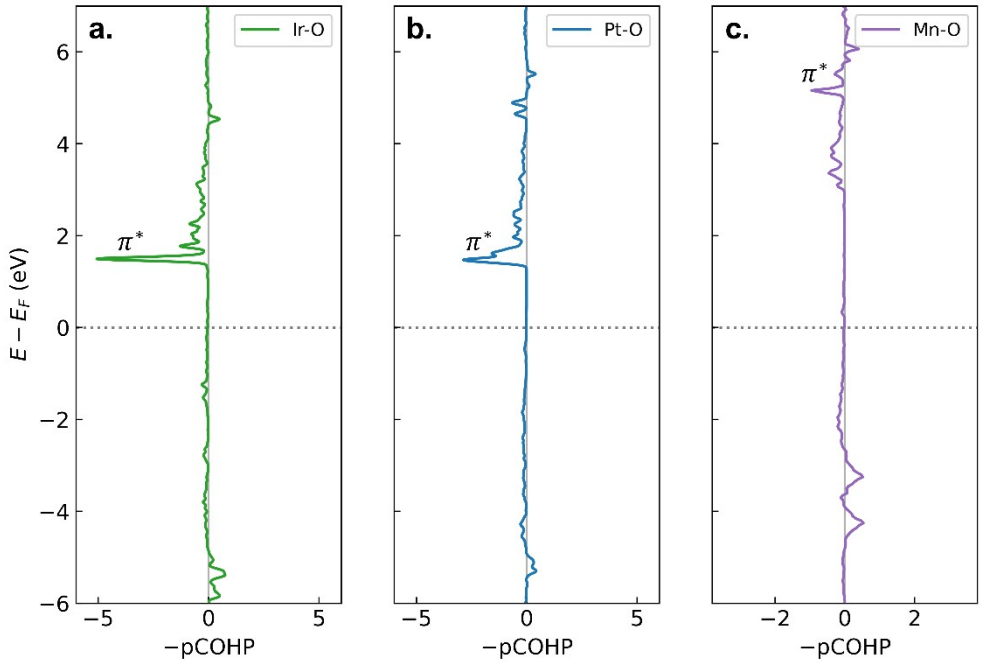

Figure S5. –pCOHP plots for M–O bond of the CH_3OH adsorbed on (a) $IrO_2(110)$, (b) β-$PtO_2(110)$, and (c) β-$MnO_2(110)$ surfaces. Positive and negative –pCOHP values indicate bonding and antibonding interactions, respectively.

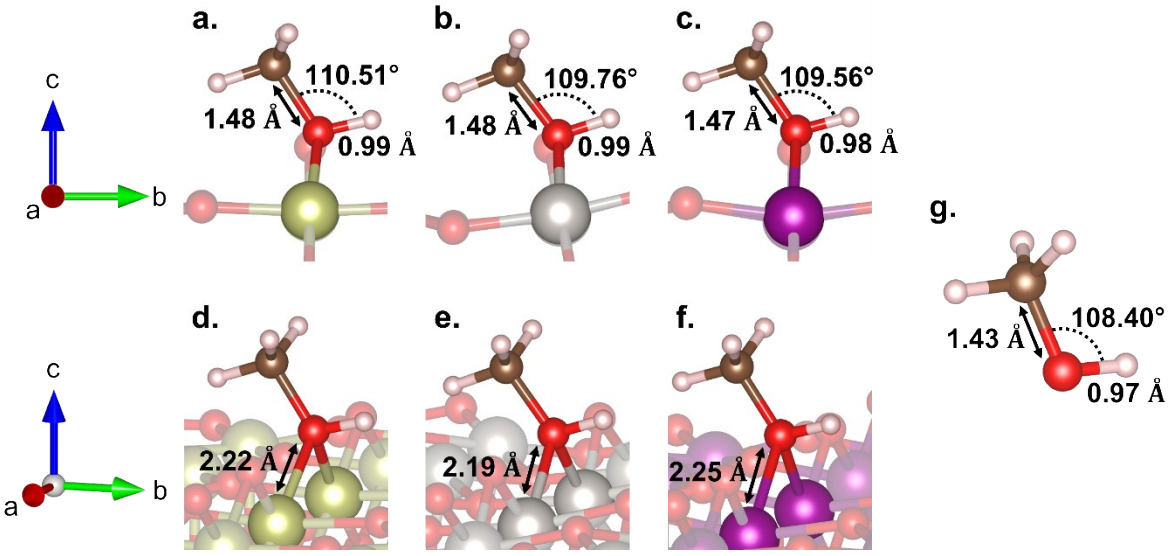

Figure S6. Geometrical parameters of the formed methanol adsorbed on the stoichiometric (a, d) $IrO_2(110)$, (b, e) β-$PtO_2(110)$, and (c, f) β-$MnO_2(110)$ surfaces, and (g) that in the gas phase.

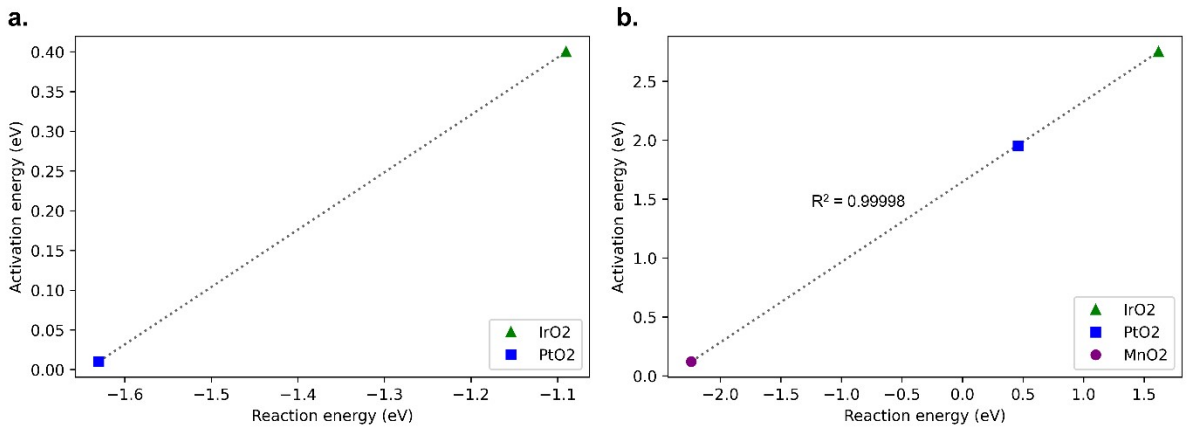

Figure S7. Plots of E_a vs. ΔE for the (a) C–H activation and (b) HO–CH_3 formation steps.

In plot (a), since the C–H activation mechanism on the β-MnO_2(110) (homolytic mechanism) is different from that on the IrO_2(110) and β-PtO_2(110) (heterolytic mechanism), we cannot include the E_a and ΔE of the β-MnO_2(110) to the plot. Thus, the BEP relation in this case (with only two points of data) seems unreliable.

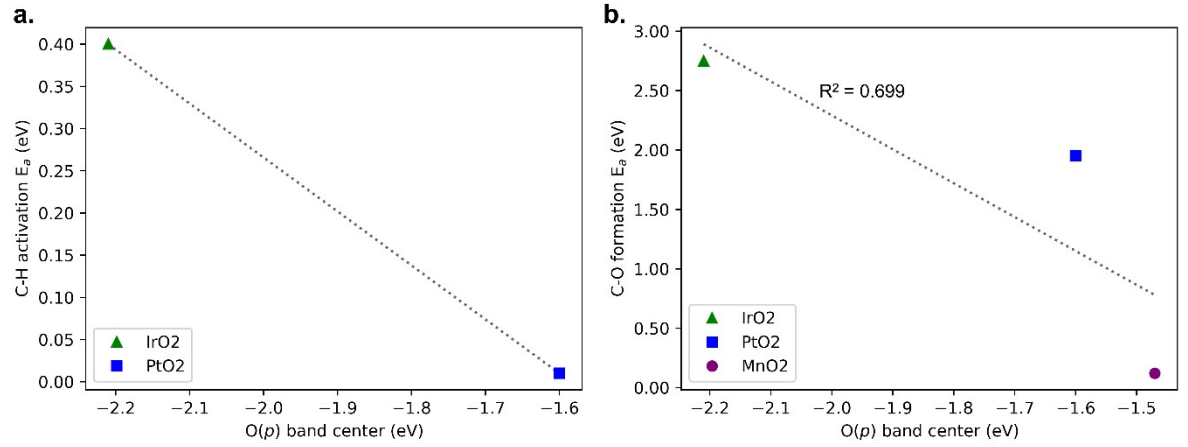

Figure S8. Plots of E_a of (a) C–H activation and (b) HO–CH_3 formation steps against the O p-band center of the clean IrO_2(110), β-PtO_2(110), and β-MnO_2(110) surfaces.

In plot (a), since the C–H activation mechanism on the β-MnO_2(110) (homolytic mechanism) is different from that on the IrO_2(110) and β-PtO_2(110) (heterolytic mechanism), we cannot include the E_a(C–H) and O p-band center of the β-MnO_2(110) to the plot. Thus, the relation in this case (with only two points of data) seems unreliable. In plot (b), the coefficient of determination (R^2), is found to be low, suggesting a low dependency of the HO–CH_3 formation on O p-band center.

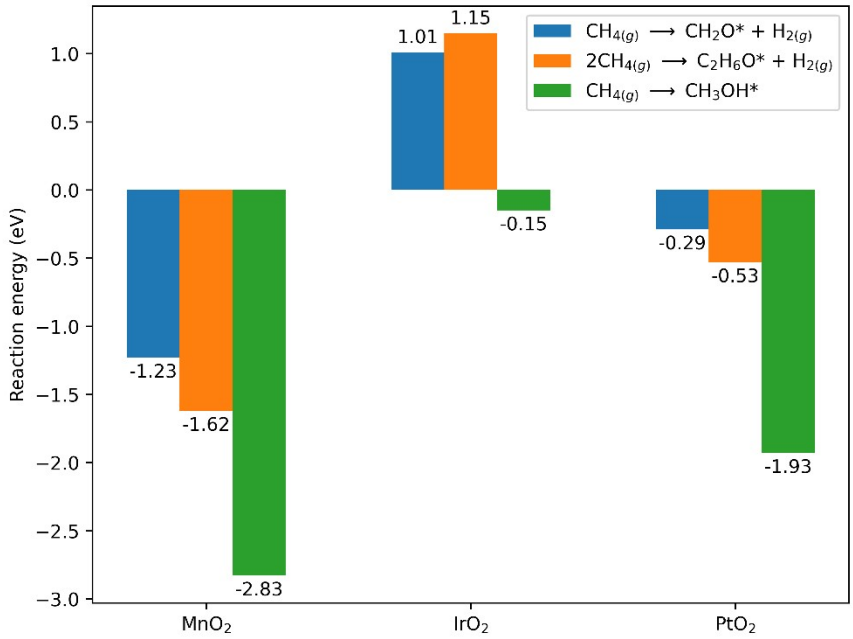

Figure S9. Comparison of reaction energies for the CH_3OH^*, CH_2O^*, and $C_2H_6O^*$ formation, showing a higher stability of CH_3OH formation as compared to the formation of the other two side products as a result of overoxidation.

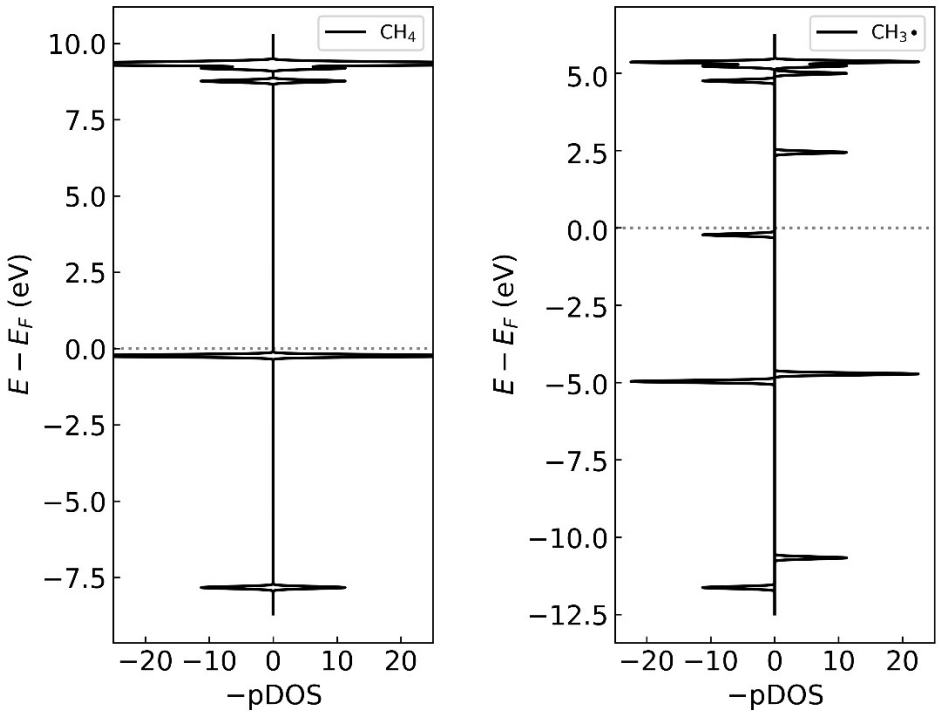

Figure S10. Total DOS of CH_4 and $\bullet CH_3$ in the gas phase (isolated in big vacuum).

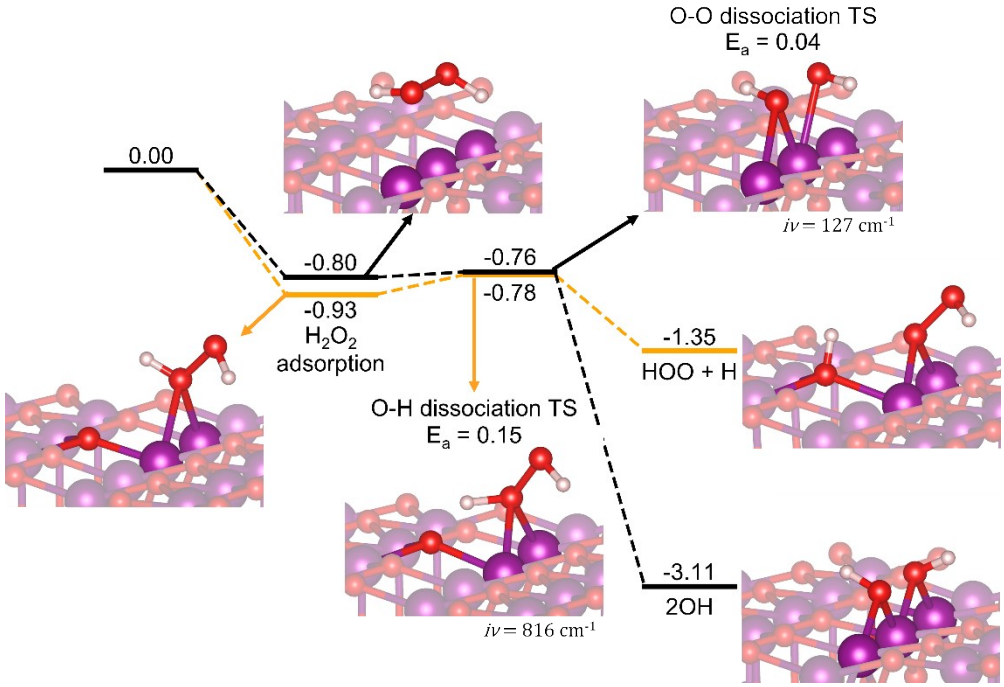

Figure S11. Energy diagrams (in eV) of H_2O_2 decomposition on the reduced β-MnO_2(110) surface via the O–O and O–H bond scission pathways.

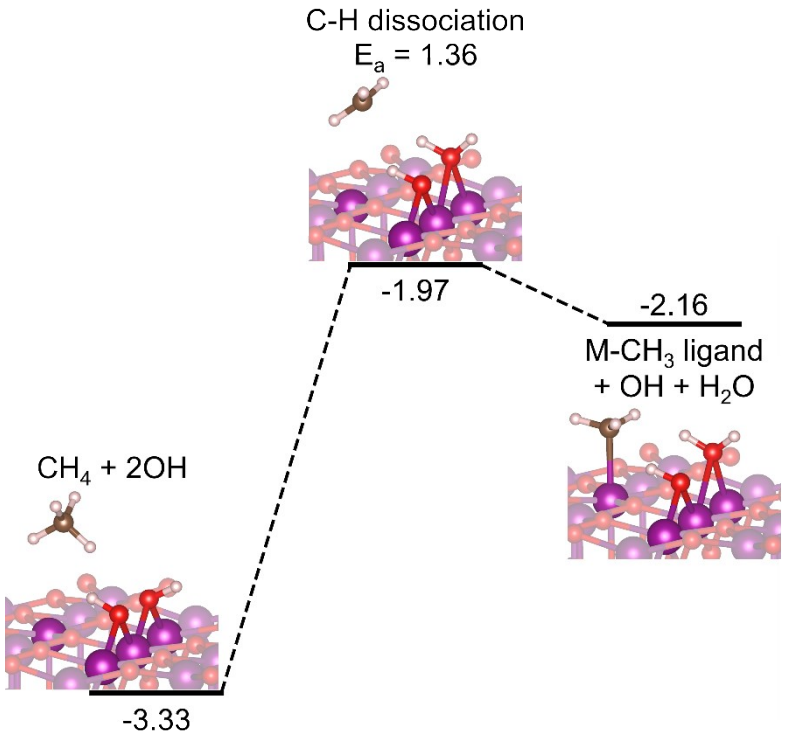

Figure S12. Energy diagrams (in eV) of H–CH_3 bond scission on the reduced β-MnO_2(110) surface via a mechanism that leads to the Mn–CH_3 formation.

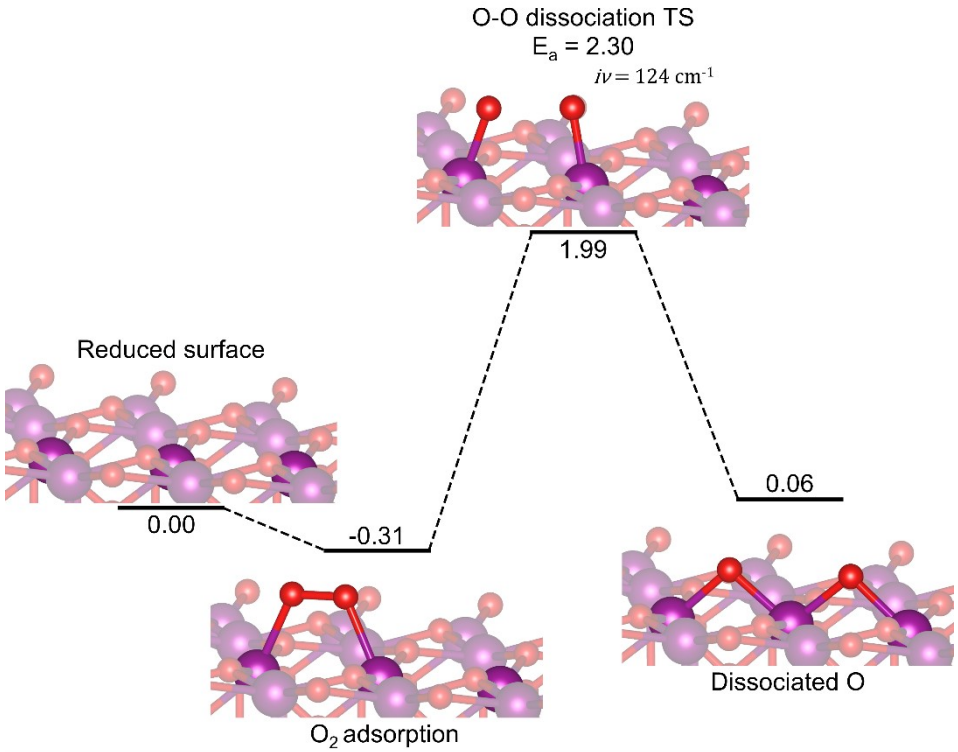

Figure S13. Energy diagram (in eV) of O_2 dissociation on the reduced β-MnO_2(110), forming back the fresh stoichiometric β-MnO_2(110) surface.